Biophysical Journal, Volume *115*

Supplemental Information

Dynamic Clustering of Dyneins on Axonal Endosomes: Evidence from High-Speed Darkfield Imaging

Praveen D. Chowdary, Luke Kaplan, Daphne L. Che, and Bianxiao Cui

Dynamic clustering of dyneins on axonal endosomes - Evidence from high-speed darkfield imaging

Praveen D. Chowdary[a], Luke Kaplan[a], Daphne L. Che[a], and Bianxiao Cui[a,1]

[a] Department of Chemistry, Stanford University
380 Roth Way, Stanford, CA 94305, USA

[1] Corresponding Author: Bianxiao Cui
Email: bcui@stanford.edu

Supplementary Information: Table of Contents

1. Experiments and Data processing

2. 3D Stochastic model for multi-dynein endosome transport

1. Experiments and data processing

1.1 Single particle tracking of GNP-endosome transport in time lapse movies:

Semi-automated custom Matlab software is used to extract endosome trajectories *(X(t),Y(t))* from the time lapse movies of axonal transport as described earlier (1). Briefly, we used 2D-Gaussian fitting adapted to detect the locations of endosomes (with GNPs) in each movie frame. We then used a particle-tracking algorithm, adapted from Jaqaman et al. (2), to link these detected locations into endosome trajectories. The flux of endosome transport, kept very sparse by controlled incubation conditions, lead to minimal tracking errors. Occasional errors associated with crossing trajectories are corrected by manual inspection in the final step of processing. For each endosome trajectory, we extracted the underlying microtubule track (Q^x,Q^y) using an edge-based tracing algorithm. Using this microtubule track, the endosome trajectory is converted from camera pixels *(X(t),Y(t))* to microtubule coordinates $(Q^{||}(t),Q^{\perp}(t))$ representing the motion parallel and perpendicular to the microtubule (1). Since the microfluidic channels (and hence the axons) are aligned along the *X*-axis of the camera, *X(t)* is an approximation for $Q^{||}(t)$.

Drift correction: For GNP-endosome trajectories spanning multiple movies, we corrected for the stage drift and mechanical disturbances using stationary scattering objects within the movies as internal references. We note that these references are associated with some highly scattering structures within axons and exhibited a slow drift with time. Therefore, some residual drift even within the reference corrected GNP-endosome trajectories cannot be ruled out completely.

1.2 Localization precision of GNPs with darkfield imaging at 1 kHz:

We obtained the localization precision of our darkfield imaging system using the standard approach detailed in literature (3). Briefly, we imaged the 80 nm GNPs stuck on a coverslip surface at 1 kHz for a duration of 22 seconds and then tracked the positions of the GNPs as discussed above. In order to correct for the long-time drift in measuring the localization precision, we subtracted the coordinates of pairs of GNPs (Fig. S0A) and got the distribution of differences for each pair (Fig. S0B). The standard deviation of this distribution of differences divided by √2 gives the localization precision of 4.4 ± 0.8 nm (Mean ± SD, N = 9).

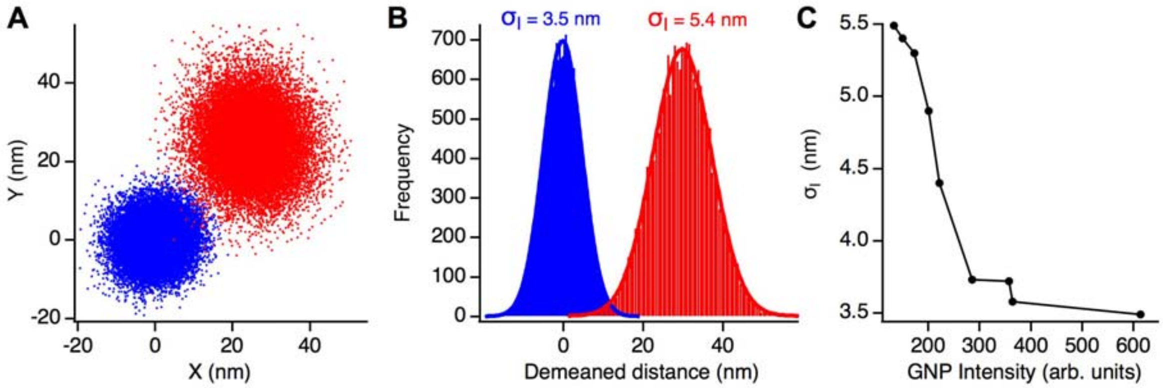

Figure S1: Localization precision (σ_I) of 80 nm GNPs with darkfield imaging. A) Referenced and demeaned position coordinates of two GNPs over 22 seconds of tracking at 1 kHz. The red distribution is offset for clarity. B) Demeaned difference distributions of the two GNPs shown in (A). The red distribution is offset for clarity. The standard deviation divided by √2 gives the localization precision σ_I. C) Localization precision as a function of the GNP intensities (spanning the range of GNP intensities in this work).

1.3 Detachment model fitting of endosome jumps:

We previously described (4) how the endosome jumps (gradual stalling followed by dynein detachment) can be explained by considering that the endosome is docked to the microtubule by an elastic tether. The dyneins pulling the tethered endosome are slowed down by the elastic restoring force of the tether ($F_{opp} = -kx$) opposing the endosome motion. The endosome gradually stalls as the tether is stretched and F_{opp} reaches the stall force of the leading dyneins. When the stalled dyneins detach from the microtubule, the endosome recoils back under the influence of F_{opp}. We also presented a model for dynein detachment under the elastic tether load to fit the post detachment recoil profiles of endosome jumps (4). Our model shows that the recoil profile is an exponential with a damping constant k/γ, where k is the tether stiffness and γ is the friction coefficient of the medium. Specifically, the endosome recoil is described by Eq. S1, where t_d is the detachment time, V_{detach} is the instantaneous recoil velocity of endosome at detachment, and k/γ is the damping constant. By fitting the single-endosome jumps with uninterrupted recoil profiles, we can obtain the damping constant k/γ for the endosome.

$$q(t) = q_s + \frac{C}{D}\left(1 - \exp\left(-D(t - t_d)\right)\right); \quad C = V_{\mathrm{det}ach}; \quad D = \frac{k}{\gamma}; \; t > t_d \qquad \text{(S1)}$$

1.4 Maximum frame velocity and Instantaneous detachment velocity:

The endosome trajectory in Fig. 2 of main text (acquired at 100 fps) exhibited ~500 stalls and detachments over a time of 18 minutes. However, the recoil profile following motor detachment is often interrupted within 30 – 40 ms, possibly by lagging microtubule-bound dyneins or fast rebinding of detached dyneins. In such cases, with a limited recoil range of 3 – 4 time points, fitting the exponential form in Eq. S1 would lead to inaccurate fit parameters (V_{detach} and k/γ). We therefore used the maximum frame velocity (V_{maxf}), which is easy to compute, as a simple statistical metric to compare the model simulations and experiment in this work. The maximum frame-to-frame velocity ($<V_{detach}$) is correlated to the instantaneous detachment velocity (V_{detach}) depending on the imaging frame rate and the damping constant k/γ of the recoil profiles. We simulated hundreds of recoil profiles using Eq. S1, with a wide range of V_{detach} values and fixed k/γ, and digitized the profiles at 100 Hz. We then extracted the V_{maxf} for each of these profiles and observed a linear relationship (that depends on frame rate and k/γ) between V_{maxf} and V_{detach}.

1.5 Automated detection and quantification of sequential endosome jumps:

In order to quantify the sequential stalls and detachments in the experimental and simulated trajectories, we used the following automated routine. First, we used a sliding window of 0.5s to identify the extrema (minima and Maxima) in the endosome trajectory. In cases where there are two successive minima (or Maxima), we identified the missed intermediate maximum (or minimum) in the second step. These steps successfully identified each of the endosome jumps as a minimum-Maximum-minimum (m-M-m) sequence in the trajectory as shown in Fig. S1. We then identified the detachment point within each m-M-m sequence as the time point preceding the time-point with the maximum frame-to-frame velocity. Finally, we selected only those m-M-m sequences that exhibited the recoil for at least two successive frames following the detachment point as valid endosome jumps. This step removes the spurious m-M-m sequences with no obvious motor detachment. We then computed the histograms of the variables like stall duration, detachment duration, and recoil duration for each endosome jump as shown in Fig. 3 (main text).

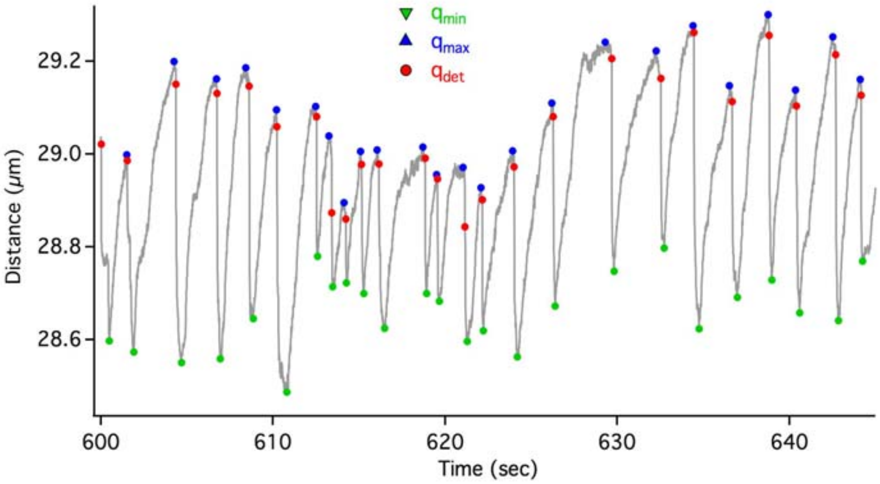

Figure S2: Automated detection of the maximum (q_{max}), minimum (q_{min}), and detachment (q_{det}) positions within endosome jumps. Experimental trajectory from Fig. 2 of main text.

1.4 Single endosome motility under load imaged at 500 fps:

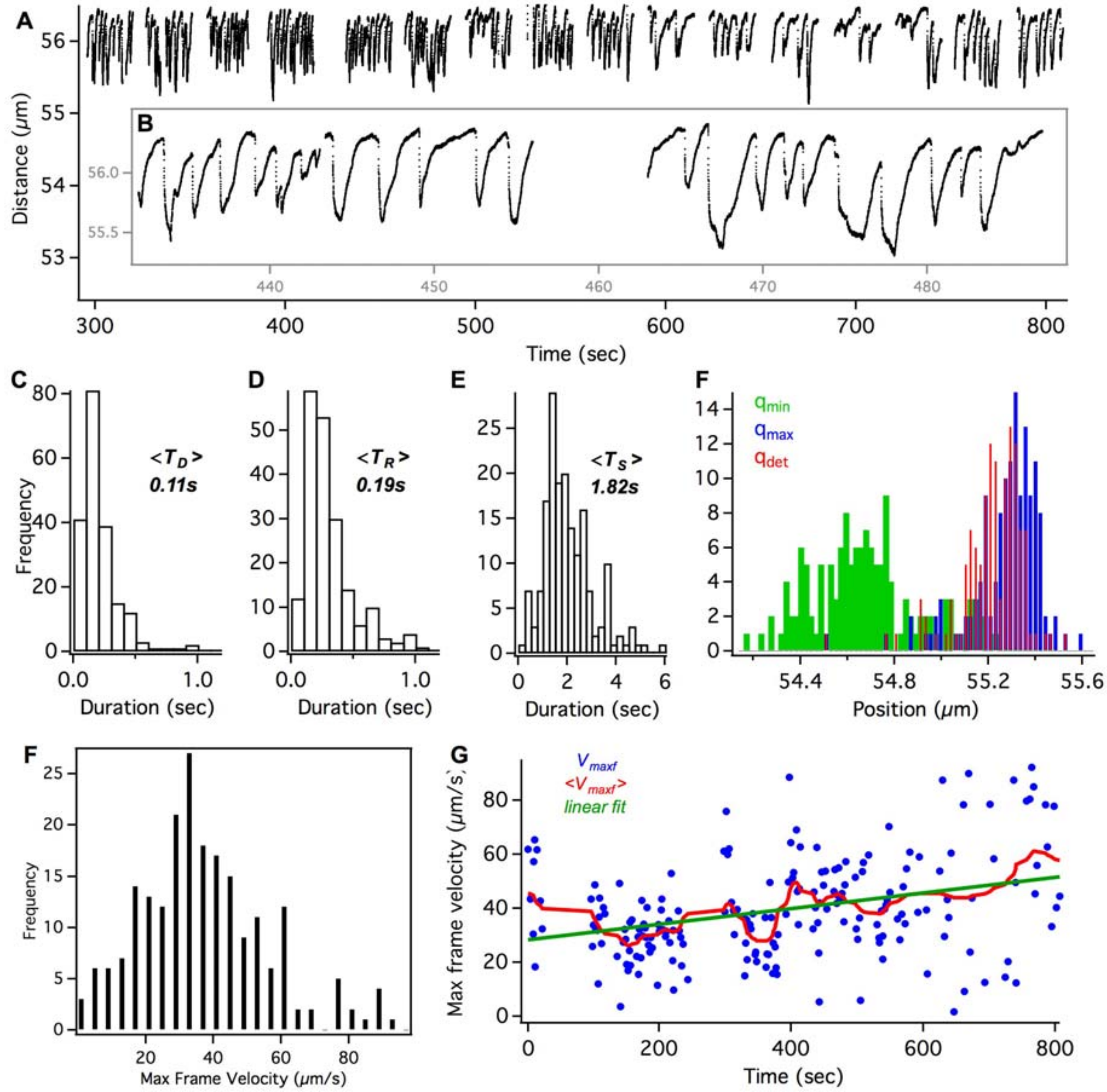

Figure S3: Single endosome dynamics under load imaged at 500 fps for over 14 minutes. A) Repeated stalls and detachments (~200) of a retrograde moving endosome. B) zoomed view of the endosome jumps. The distributions of T_D, T_R, and T_S for the simulated endosome jumps are shown in C), D), and E) respectively. F) Histograms of q_{min}, q_{max}, and q_{det} positions from the endosome jumps (check Fig. 3A for variable definitions). F) The distribution of V_{maxf} obtained from all the endosome jumps. G) Stochastic and dynamic variations in V_{maxf} with time. The blue markers show V_{maxf} for each individual jump, the red line shows 51-point smoothed $<V_{maxf}>$, and the green line is a linear fit.

2. 3D stochastic model for multiple dynein endosome transport

2.1 3D stochastic mechanical model:

Multi-motor 1D mechanical models for cargo transport, based on Monte Carlo simulation of cargo trajectories, have been elaborated for different motility regimes in literature (5-7). Erickson et al. have also presented a prototypical 3D stochastic model for cargo transport by multiple kinesins (8). Our 3D stochastic model, for endosome transport by multiple dyneins, is based on this prototype with key modifications in modeling the mechanochemical properties and the spatial distribution of dyneins on endosomes. Here we briefly summarize the general characteristics as well as the details specific to our 3D model.

We modeled the endosome as a hard sphere (radius R) driven by a stable number of endosome-bound dyneins (N_d) walking on a microtubule (along *x*-axis of lab frame) in 8 nm steps. The dyneins are distributed either in a random or clustered geometry on the endosome and when geometrically possible the dyneins can repeatedly bind to (rate = π/s) and detach from (rate = ε/s) the microtubule. At any instant, the dyneins engaged on microtubule can step forward (k_f/s) or backward (k_{back}/s), or detach (ε/s) from the microtubule with well-defined rates given below. The motors are treated as harmonic springs that exert a restoring force $f = -k(l-l_0)$ and torque on the endosome when stretched beyond their rest length l_0. The dynein-endosome contact positions are either rigidly fixed or allowed to diffuse and slide under torque on the endosome surface. At any instant, the endosome position/orientation is determined by the net force/torque exerted by dyneins and the thermal forces (see below).

The 3D motion of endosome can be separated into translational and rotational components as follows. Briefly, the translational motion of the endosome center of mass is described in terms of the laboratory frame *(x, y, z)* with the microtubule modeled simply as a 1D lattice of 8nm steps along the *x*-axis. The rotational motion is described in terms of the endosome frame of reference *(a, b, c)* related to the lab frame by Euler angles ($\theta(t)$, $\phi(t)$, $\psi(t)$) according to the *x*-convention. In what follows, we present the relevant equations for translational and rotational motion derived in detail by Erickson et al (8) and the procedure for dealing with dynein-endosome contact motion on the endosome surface.

2.2 Translational Motion:

The translational motion of the endosome center of mass is governed by Eq. S2, where $v(t)$ is the instantaneous velocity of endosome, γ_T is the friction coefficient of the medium, and $F_{th}(t)$ is the random thermal force on endosome.

$$m\frac{d\vec{v}(t)}{dt} = -\gamma_T\vec{v}(t) + \vec{F}(\vec{q},t) + \vec{F}_{Th}(t); \quad \gamma_T = 6\pi\eta R$$

$$\vec{F}(\vec{q},t) = k\sum_{i=1}^{M_d}\left(l_i(\vec{q},t) - l_i^0\right)\bullet\hat{l}_i(\vec{q},t) + \vec{F}_{ext}(\vec{q}) \qquad \text{(S2)}$$

F(q,t) is the net force on endosome obtained as the sum of forces exerted by the stretched dyneins ($M_d \leq N_d$) and any other external force on endosome. Solving Eq. S2, it can be shown that (8) the stochastic displacement of endosome center of mass over a time step *dt* is given by Eq. S3, where σ_T is the translational diffusion length and $\vec{\varepsilon} = (\varepsilon_x, \varepsilon_y, \varepsilon_z)$ is a vector of independent standard normal deviates. While the second term on the right hand side represents the drift of endosome under net force, the third term represents the random thermal motion of the endosome.

$$\vec{q}(t+dt) \approx \vec{q}(t) + \frac{dt}{\gamma_T}\vec{F}(\vec{q},t) + \sigma_T\vec{\varepsilon}; \quad \sigma_T = \sqrt{\frac{2k_bT}{\gamma_T}dt} \qquad \text{(S3)}$$

2.3 Rotational Motion:

The rotational motion of the endosome is governed by Eq. S4 which is the torque equation in the lab frame, where *w(t)* is the instantaneous angular velocity of endosome, γ_R is the rotational friction coefficient, and $\vec{\tau}_{Th}$ is the random torque on endosome.

$$I\frac{d\vec{w}(t)}{dt} = -\gamma_R\vec{w}(t) + \vec{\tau}(\vec{q},t) + \vec{\tau}_{Th}(t); \quad \gamma_R = 8\pi\eta R^3$$

$$\vec{\tau}(\vec{q},t) = k\sum_{i=1}^{M_d}\vec{R}_i(\vec{q},t)\times\left(l_i(\vec{q},t) - l_i^0\right)\bullet\hat{l}_i(\vec{q},t) + \vec{\tau}_{ext}(\vec{q}) \qquad \text{(S4)}$$

$\vec{\tau}(\vec{q},t)$ is the net torque on endosome obtained as the sum of torques exerted by stretched dyneins ($M_d \leq N_d$) and any other external torque on endosome. Solving Eq. S4, it can be shown that (8) the stochastic rotational motion of endosome over a time step *dt,* in terms of Euler angles, is given by Eq. S5, where σ_R is the rotational diffusion angle over the time step *dt* and $\left(\varepsilon_\theta, \varepsilon_\phi, \varepsilon_\psi\right)$ are independent standard normal deviates.

$$\theta(t+dt) = \theta(t) + \frac{dt}{\gamma_R}\left(\tau_x(\vec{q},t)\cdot\cos\phi(t) + \tau_y(\vec{q},t)\cdot\sin\phi(t)\right) + \sigma_R\varepsilon_\theta$$

$$\phi(t+dt) = \phi(t) + \frac{dt}{\gamma_R}\left(\tau_z(\vec{q},t) + \left[-\tau_x(\vec{q},t)\cdot\sin\phi(t) + \tau_y(\vec{q},t)\cdot\cos\phi(t)\right]\cdot\cot\theta(t)\right) + \sigma_R\varepsilon_\phi$$

$$\psi(t+dt) = \psi(t) + \frac{dt}{\gamma_R}\frac{\left(\tau_x(\vec{q},t)\cdot\sin\phi(t) - \tau_y(\vec{q},t)\cdot\cos\phi(t)\right)}{\sin\theta(t)} + \sigma_R\varepsilon_\psi$$

$$\sigma_R = \sqrt{\frac{2k_bT}{\gamma_R}dt} \tag{S5}$$

2.4 Motion of dynein-endosome contacts on endosome surface:

Our 3D model also considers the mobility of dynein-endosome contact positions on the endosome surface. Though the 2D diffusion of protein/lipid microdomains on cell membranes is expected to be confined or anomalous, treating this as a Brownian diffusion process is reasonable within the accuracy of our model simulations. We therefore considered that the dynein-endosome contacts can undergo Brownian diffusion on endosome surface with an effective diffusion constant D_M (typically 0.01 – 1 $\mu m^2/s$ on cell membranes, which is equivalent to 0.01/R – 1/R $radian^2/s$, where R is the endosome radius). Further, the dynein-endosome contact can also slide on the endosome surface under torque when dynein is stretched beyond its restlength. The friction coefficient for this membrane diffusion/sliding process is given by $\gamma_M = k_bT / D_M$ and the equations of motion for this process can be obtained as follows.

Consider the dynein-endosome contact point A sliding under torque on the endosome surface while the endosome orientation is fixed. The coordinates of point A over time can equivalently be obtained by assuming that the point A is fixed on the endosome surface and the endosome is undergoing rotational motion with rotational drag constant γ_M (instead of γ_R in Eq. S5). The stochastic motion of the dynein-endosome contact position over a time step dt can therefore be determined using the equivalent changes in Euler angles given by Eq. S6 (analogous to Eq. S5) See the Monte Carlo simulation algorithm below for details.

$$d\theta(t) = \theta(t+dt) - \theta(t) = \frac{dt}{\gamma_M}\left(\tau_x(\vec{q},t)\cdot\cos\phi(t) + \tau_y(\vec{q},t)\cdot\sin\phi(t)\right) + \sigma_M\varepsilon_\theta$$

$$d\phi(t) = \phi(t+dt) - \phi(t) = \frac{dt}{\gamma_M}\left(\tau_z(\vec{q},t) + \left[-\tau_x(\vec{q},t)\cdot\sin\phi(t) + \tau_y(\vec{q},t)\cdot\cos\phi(t)\right]\cdot\cot\theta(t)\right) + \sigma_M\varepsilon_\phi$$

$$d\psi(t) = \psi(t+dt) - \psi(t) = \frac{dt}{\gamma_M}\frac{\left(\tau_x(\vec{q},t)\cdot\sin\phi(t) - \tau_y(\vec{q},t)\cdot\cos\phi(t)\right)}{\sin\theta(t)} + \sigma_M\varepsilon_\psi$$

$$\gamma_M = \frac{k_bT}{D_M} \quad and \quad \sigma_M = \sqrt{2D_M dt} \tag{S6}$$

2.5 Mechanochemical properties of dyneins:

Forward/backward stepping rates of dynein

The restlength l_0 of dynein is nominally considered to be 70 nm, while the motor stiffness k is 0.32 pN/nm and the step length d is 8 nm. We modeled the forward and backward stepping rates of dynein in two different ways using 1) a model based on the experimental force-velocity curve from in vitro measurements (9), and 2) an approximate analytical model.

Experimental model: The forward stepping rate as a function of load is modeled by the exponential decay in Eq. S7 where v_f^0 is the unloaded motor velocity, f the load on motor, and F_s the motor stall force. Though, the load dependence of dynein backward stepping rate is not explicitly reported, superstall measurements in optical traps (5, 9) show minimal backward motion even at a load of 10 pN. Therefore, we modeled the backward stepping rate using a shallow exponential given by Eq. S7, where $\Gamma = 40$ reflects the unloaded backward stepping rate of dynein seen in experiments. The exponential factors C_1, C_2 are determined by requiring that a) the forward stepping rate is equal to the backward stepping rate at the motor stall force ($f = F_s$), and b) the net velocity as a function of load fits the experimental force-velocity curve of dynein (9).

$$k_f = {}^{v_f}\!/_{d}; \quad v_f = v_f^0 \exp(-C_1 * f) \qquad \text{(S7)}$$

$$k_{back} = \frac{v_b}{d}; \quad v_b = \frac{v_f^0}{\Gamma}\exp(C_2 * f)$$

Analytical model: The forward stepping rate is modeled by Eq. S8 where v_f^0 is the unloaded motor velocity, f the load on the motor, F_s the motor stall force, and $n = 0.5$ is the nonlinearity. The backward stepping rate is modeled by a slow rising exponential given by Eq. S8, where $\Gamma =$ 40 reflects the unloaded backward stepping rate of dynein seen in experiments. In earlier studies the detachment rate is modeled using a similar functional form with $C_2 = 1/F_d$, where F_d is the detachment scale (see below).

$$k_f = {}^{v_f}\!/_{d}; \quad v_f = v_f^0\left(1-\left({}^{f}\!/_{F_s}\right)^n\right) \qquad \text{(S8)}$$

$$k_{back} = \frac{v_b}{d}; \quad v_b = \frac{v_f^0}{\Gamma}\exp(C_2 * f)$$

Detachment kinetics of dynein

In vitro measurements show that dynein exhibits an exponential detachment rate under load till its stall force and catch-bond detachment kinetics above the stall force (5, 9). The functional form of dynein detachment kinetics is therefore parametrically dependent on the stall force of dynein. For the in vitro model (1.25 pN stall force of dynein) in this manuscript, we modeled the detachment rate ε based on the in vitro catch-bond detachment kinetics from Kunwar et al. (5) given by Eq. S9, where ε^0 is the unloaded detachment rate and F_d is the detachment scale.

$$\varepsilon = \varepsilon^0 \exp\left({}^{f}\!/_{F_d}\right); f < F_s \quad \& \quad \varepsilon = \varepsilon^0\left(0.254 * \left(1-\exp\left({}^{-f}\!/_{1.96646}\right)\right)\right)^{-1}; f \geq F_s \qquad \text{(S9)}$$

We also tried the single rate exponential kinetics given by Eq. S10 for all values of f. For the in vivo model (2.5 pN stall force of dynein) in this manuscript, we modeled the detachment rate ε based on the single rate exponential kinetics given by Eq. S10.

$$\varepsilon = \varepsilon^0 \exp\left(f \middle/ F_d \right) \tag{S10}$$

2.6 Monte Carlo simulation algorithm:

Monte Carlo simulation – Initiation:

For a given endosome size (radius R), the number of dyneins (N_d), and spatial distribution of dyneins (Random or Cluster angle Θ) the simulation is initiated as follows.

1. Start the simulation with the endosome positioned 15nm above origin on the z-axis of the lab frame (x, y, z) at time 0. The endosome frame (a, b, c) is initially aligned to lab frame with the Euler angles $(0, 0, 0)$. The microtubule lattice of 8nm steps is set along x-axis.
2. Attach N_d dyneins (cargo binding ends) on endosome surface in a random or clustered geometry as described above. For random distribution, the dynein-endosome contacts are randomly distributed on the endosome surface. For clustered distribution, the dynein-endosome contacts are randomly distributed on a spherical sector of the endosome surface subtending an angle Θ (range of 0 to π radians) at the center of the endosome.
3. The geometrically active dyneins (i.e. dyneins that can reach the microtubule without stretching beyond restlength or passing through the endosome) are then attached to randomly chosen microtubular sites accessible within the restlength of motors.

Monte Carlo simulation – Propagation:

We then continuously update the states (i.e. bound or unbound to microtubule) of dyneins, the positions of dyneins on microtubule, dynein-endosome contact positions on endosome surface, and the position/orientation of endosome at each time step (dt = 0.5μs) in the following sequence.

4. Check the motor extensions and compute the force exerted by each motor (i.e the load on each motor). These are used to compute the forward/backward stepping and detachment rates for each dynein in the following step.
5. Loop through each dynein on the endosome and take one of the following actions if the dynein is bound to the microtubule.
    - Step 8nm forward with probability $P = k_f * dt$
    - Step 8nm backward with probability $P = k_b * dt$
    - Detach from microtubule and relax to restlength with probability $P = \varepsilon * dt$
    - Remain at the same position if none of the above happens

If the dynein is not bound to microtubule and is geometrically active (i.e. can reach the microtubule without passing through endosome) then, attach it to a random microtubular site accessible within its restlength with probability $P = \pi * dt * \xi$, where ξ is the ratio of the number of accessible microtubular sites to the maximum number of accessible sites for the motor length given by $2l_0/8$.

6. [Optional step when simulating endosome motility against the load of an elastic tether]. If the current simulation time is greater than a preset duration (typically 10s) and the closest distance between the endosome and the microtubule is less than a preset tether length L_T, then connect the closest points on the endosome and microtubule with an elastic tether of length L_T and stiffness k. If a tether is already established, then ignore this step.
7. If all motors are detached and the endosome is not connected to the microtubule anymore (i.e. no external tether), then randomize the endosome orientation, and reattach the geometrically active dyneins to microtubule as in step 3.
8. Update all the states (bound or unbound) and positions of the motors on the microtubule simultaneously.
9. Compute the motor extensions and the force exerted by each dynein on the endosome. Compute the external force (i.e. from any elastic tether connecting the endosome and the microtubule as discussed below). Compute the net force on the endosome using Eq. S2.
10. Compute the new position of the endosome center of mass using Eq. S3.
11. Compute the torques exerted at each of the dynein-endosome contact. Compute the external torque (i.e. from any elastic tether connecting the endosome and the microtubule as discussed below). Compute the net torque on the endosome using Eq. S4.
12. For each dynein-endosome contact under torque, compute the equivalent changes in the Euler angles of endosome representing the displacement of the dynein-endosome contact on the endosome surface using Eq. S6. Perform a rotational transformation of the dynein-endosome contact position using these angles to obtain the new position of the dynein-endosome contact on the endosome surface. Update all the new positions of the dynein-endosome contact positions simultaneously.
13. Compute the changes in the Euler angles of the endosome due to the net torque computed in step 10 using Eq. S5.
14. Update the new position and orientation of the endosome.
15. Following an initial stabilization period of around 5 – 10s, start recording the averages of relevant variables (endosome center of mass position, endosome orientation, number of motors cooperatively driving the transport etc.) at an acquisition rate equivalent to the experimental imaging rate (100 – 500 Hz).
16. Repeat steps 4 – 14 till the any of the simulation termination conditions are met.

Monte Carlo simulation – Termination:

The simulation is terminated when any of the following termination conditions is met and the recorded variables are saved for subsequent analysis.

17. The simulation is terminated when the simulation time exceeds the initially set time duration in the range of 5 – 20 minutes, or optionally if the distance covered by the endosome exceeds the camera field of view.
18. Finally, we add Gaussian noise ($\sigma = 5 – 10$nm) to the simulated trajectory (position of the endosome center of mass) to replicate the localization accuracy of our system.

2.7 Simulation of endosome stalls and detachments – Load from elastic tether:

As mentioned above, the endosome stalls and detachments can be explained by considering that the endosome is docked to microtubule by an elastic tether that exerts load when stretched. In order to simulate the endosome stalls and detachments, we therefore modeled the opposing load as resulting from an elastic tether docking the endosome to the microtubule. Briefly, we start with an endosome being driven by N_d dyneins. After a preset duration (typically 10s) of unloaded transport, we suddenly establish a physical tether of nominal length L_T = 50 nm and stiffness k between the endosome and microtubule as explained in step 6 of Monte Carlo simulation algorithm. The tether buckles freely under pressure but exerts a restoring force $F_{ext} = -k*(L-L_T)$ when stretched beyond L_T (included in Eq. S2).

Fig. 5A (main text) shows a simulated trajectory of an endosome repeatedly stalling against such elastic load and detaching from the microtubule. The endosome stall and recoil profiles depend on the number of motors, their binding rate, their unitary stall force, and the load dependence of their velocity and detachment kinetics.

3. Stochastic model simulations

3.1 Estimating model parameters from single-endosome experimental data:

For an endosome with tens of sequential stalls/detachments, many of the model parameters can be determined from the experimental data. Here, we present the parameter estimation for the endosome with multiple jumps shown in Fig. 2 of main text.

1. The forward and backward stepping rates of dynein are estimated using the run velocity of the endosome before exhibiting stalls and detachments based on the details given above (Eq. S8.)
2. Based on the peak multiplicity (110 – 120 nm) in the jump size and detachment velocity distributions we estimated the involvement of ~ 8 dyneins on the endosome.
3. Considering the 110 nm as the stall size of a single dynein, the tether stiffness k is estimated as $k=Fs/110$ pN/nm, where Fs is the stall force of dynein.
4. We then selected a few endosome jumps with near-exponential recoil profiles and fit them to Eq. S1 to obtain $k/\gamma = 81 \pm 6.7$/s for 65 jumps with <10% fit error.
5. The friction coefficient γ is then obtained as $\gamma = F_s*0.001/(110*81)$ Ns/m
6. The effective axonal viscosity for endosomes is estimated as $\eta \sim 0.1$ Ns/m^2.
7. We then estimated the radius of the endosome as $R = \gamma/6\pi\eta$. From these considerations we obtained the following initial parameter estimates for the model simulations.

In vitro model (F_s = 1.25 pN): Rd = 75, 149 nm for η = 0.1, 0.05 Ns/m^2 respectively.

High stall force model (2.5 pN): Rd = 75, 149, 298 nm for η = 0.2, 0.1, 0.05 Ns/m^2 respectively.

All the simulations in Table 1 (main text) were run with the endosome radius 75 nm. The assumption of a single dynein per 110 nm stall size gives an initial estimate for the number of active dyneins on the endosome. However, we have also explored a wide range of parameters in our model simulations around these initial estimates. For instance, while the initial estimate based on Fig. 2B was 8 dyneins, the motor number is varied from 6 – 14 in model simulations and the best result is considered for any given model in Table 1. Our intention was to ensure that a model failure was not due to an incorrect initial estimate for the motor number. While the high stall force model with exponential kinetics gave a good fit with the initial estimate of 8 – 10 motors, the in vitro model (with in vitro detachment kinetics) fared poorly over this entire range of parameters. However, the high stall force model with exponential kinetics fit the experimental data with minimal modification of the experimentally estimated parameters. We note that the results of model simulations were negligibly affected within the range of 110 – 120 nm for single dynein stall size.

We also considered the assumption of 2 dyneins per 110 nm jump in our simulation which gives an initial estimate of ~16 active dyneins on the endosomes. This is beyond the range of the number of dyneins on neuronal vesicles reported by immunostaining studies so far. Further, for 16 dyneins to be geometrically active they need to be clustered at least within one hemisphere of the endosome. Simulations with the in vitro model under these conditions offered no improvement over the assumption of 1 dynein per 110 nm.

3.2 In vitro model simulations (clustered dynein distribution):

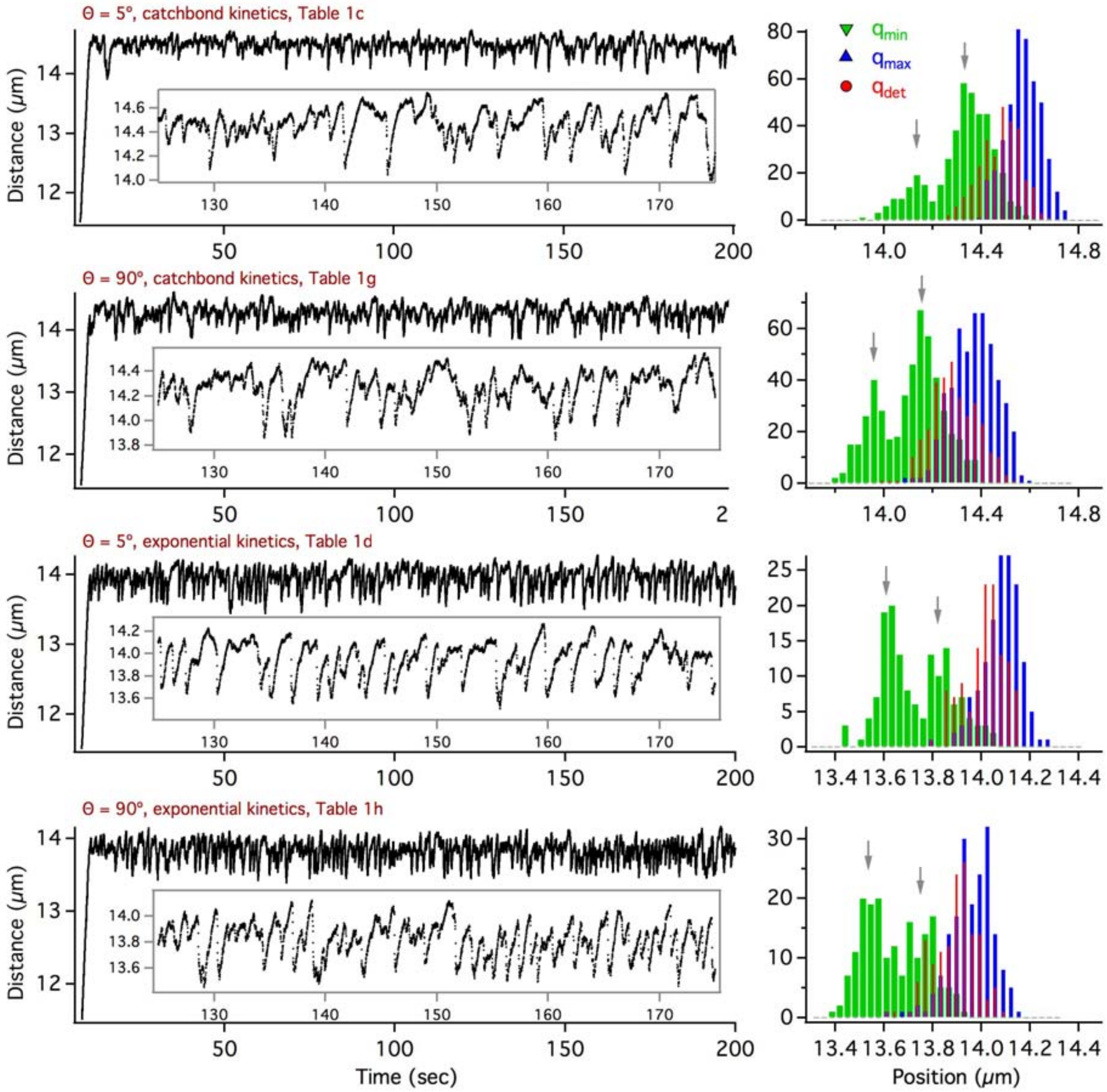

Figure S4: In vitro model simulations with clustered dynein distributions. Left Panel: Simulated trajectories, showing stalls and detachments, for different clustered geometries and detachment kinetics. Right Panel: The corresponding histograms of q_{min}, q_{max}, and q_{det} positions (as defined in Fig. 3A) from the endosome jumps in each simulated trajectory. The grey arrows highlight the bimodal distribution of q_{min}. The bimodality results from a) fast interruptions of the endosome recoil caused by the high number of geometrically active dyneins in the clustered geometry and b) the catchbond kinetics decreasing the frequency of complete motor detachment and thereby increasing the residence time of the endosome in the high load regime.

4. Statistical analysis of the peaks in experimental distributions

***Power spectrum analysis*:**

We used the power spectrum analysis to determine if there were roughly evenly spaced peaks in the jump size and maximum frame velocity distributions, corresponding to discrete numbers of active motors (Fig. S4 A,B). A probability density function of the data was obtained using kernel density estimation with a normal kernel of width 5 nm for jump size (q_d) and 0.6 μm/s for velocity (v_d) distributions. As a null hypothesis, a unimodal Weibull function was fit to the data. Control distributions were generated by bootstrapping the null hypothesis and generating power spectra to estimate a 90% confidence interval for a unimodal distribution. Frequencies above the 95th percentile of the null hypothesis were considered as statistically significant.

Figure 1 demonstrates this method for the velocity distribution (Fig. 2C of main text). Figure 1A shows simulated distributions of the velocity data by randomly sampling six evenly spaced Gaussian distributions with their means spaced 5.1 μm/s apart. If the peak width is very narrow (top panel, 0.5 μm/s) the peaks are clearly distinguishable, but as the peak width approaches the spacing, the peaks are harder to distinguish (bottom panel, 5 μm/s). The power spectral densities as a function of peak width are shown in Fig. S4B with a very prominent peak at narrow peak widths (0.5 μm/s, dark blue line) and no clear peak at large widths (5.0 μm/s, dark red line). The power spectral density of the experimental velocity data (Fig. 2C of main text) is shown in black. The peak height of the experimental data is close to that of the 3.6 μm/s wide peaks in the simulated data (middle panel of Figure 1A).

Figure 1C shows the power spectral density of the experimental data overlaid on the power spectral density of the null hypothesis Weibull fit to this data (blue line, 90% confidence intervals in gray). The power at the frequency corresponding to 5.1 μm/s is higher than the 95th percentile of the unimodal fit.

The same analysis applied to the jump size distribution (Fig. 2B of main text) confirmed the statistical significance of peaks with an approximate spacing of 120 nm.

Maximum likelihood estimation of peak spacing in v_d and q_d distributions:

As a separate method for determining the peak spacing, the distributions of v_d and q_d were fit to a Gaussian mixture model where each Gaussian is defined by a position, width, and amplitude. In our model, each Gaussian represents the discrete number of motors pulling the endosome prior to the detachment, so the spacing between successive Gaussians is the contribution of a single motor unit. Therefore, instead of independently assigning a position, width, and amplitude to each peak in the distribution, we fit a single model to the whole distribution for each endosome.

The model has six parameters: the spacing between peak centers (p), the position of the first peak (μ_o), the width of each peak (σ_o), and a noise term allowing for peak broadening as more motors participated in a given jump (η). These four parameters define the position and width of each Gaussian. Two additional parameters, λ and K define the amplitude by determining the probability of a given number of motors participating in each jump. λ and K are obtained by fitting the data to a Weibull distribution where K is the shape parameter and λ is the scale parameter. In the initial Weibull fit, λ is in units of velocity or distance (for v_d and q_d respectively), which can be converted to number of motors by dividing by the spacing parameter, p (in units of velocity/motor or distance/motor for v_d and q_d respectively). It is this rescaled λ that is used in the Gaussian mixture model.

Negative log likelihood was estimated by convolving the model with each data point and its error estimated from the fitting of individual jumps, thereby accounting for differences in error across different jumps.

$$\mu_n = \mu_o + np \tag{S11}$$

$$\sigma_n = \sigma_o + \sqrt{n}\eta \tag{S12}$$

$$P(\#motors = n) = \frac{K}{\lambda}\left(\frac{n}{\lambda}\right)^{K-1} \exp\left(-\left(\frac{n}{\lambda}\right)^{K}\right) \tag{S13}$$

$$\sum_{i=1}^{\infty}\sum_{j=1}^{J} -log\left(P(i)\int_{-\infty}^{\infty} N(\mu_i,\sigma_i)N(\mu_j,\sigma_j)\,dx\right) \tag{S14}$$

Where N is the normal distribution; μ_i, σ_i are from equations S11, S12; and μ_j, σ_j are the j$^{\text{th}}$ data point from the experiment and its associated standard error with J total data points (i.e. J total jumps). This construction allows for calculation of p from all the data at once. It also means that the number of parameters in the model is fixed, irrespective of the number of peaks in the distribution. This is in contrast to a conventional Gaussian mixture model where the number of parameters grows with the number of Gaussians fit.

We found that expectation maximization was sensitive to the initial guess of p, as can often be in the case of maximum likelihood approaches. Therefore, to avoid overfitting, we performed the fit with several initial guesses of p. The initial values and upper and lower bounds are set such that the distribution is fit by increasing integer number of Gaussians starting from one going up to p = 2μm/s or p = 25nm for v_d *and* q_d respectively. For each fit, we computed the Akaike information criterion (AIC) taking the number of Gaussians in the mixture as the number of parameters.

We then used the parameter value at the AIC minimum as the initial guess for the fit, and then maximized the likelihood without the upper and lower bound constraints in MATLAB. We found that this approach worked well to avoid overfitting the distributions of v_d and q_d for the simulated trajectories where the number of motors is known. The confidence intervals of the fit were computed from the inverse of the information matrix calculated at the maximum likelihood parameter values.

Using this approach, we found the peak spacing of 119 (107, 131) nm for the jump sizes and 4.7 (4.2, 5.1) μm/s for detachment velocities (numbers in parentheses represent the 95% confidence interval). Fig. S4D,E show the Gaussian mixture model fits overlaid on the experimental distributions of jump size and maximum frame velocities (Fig. 2 of main text).

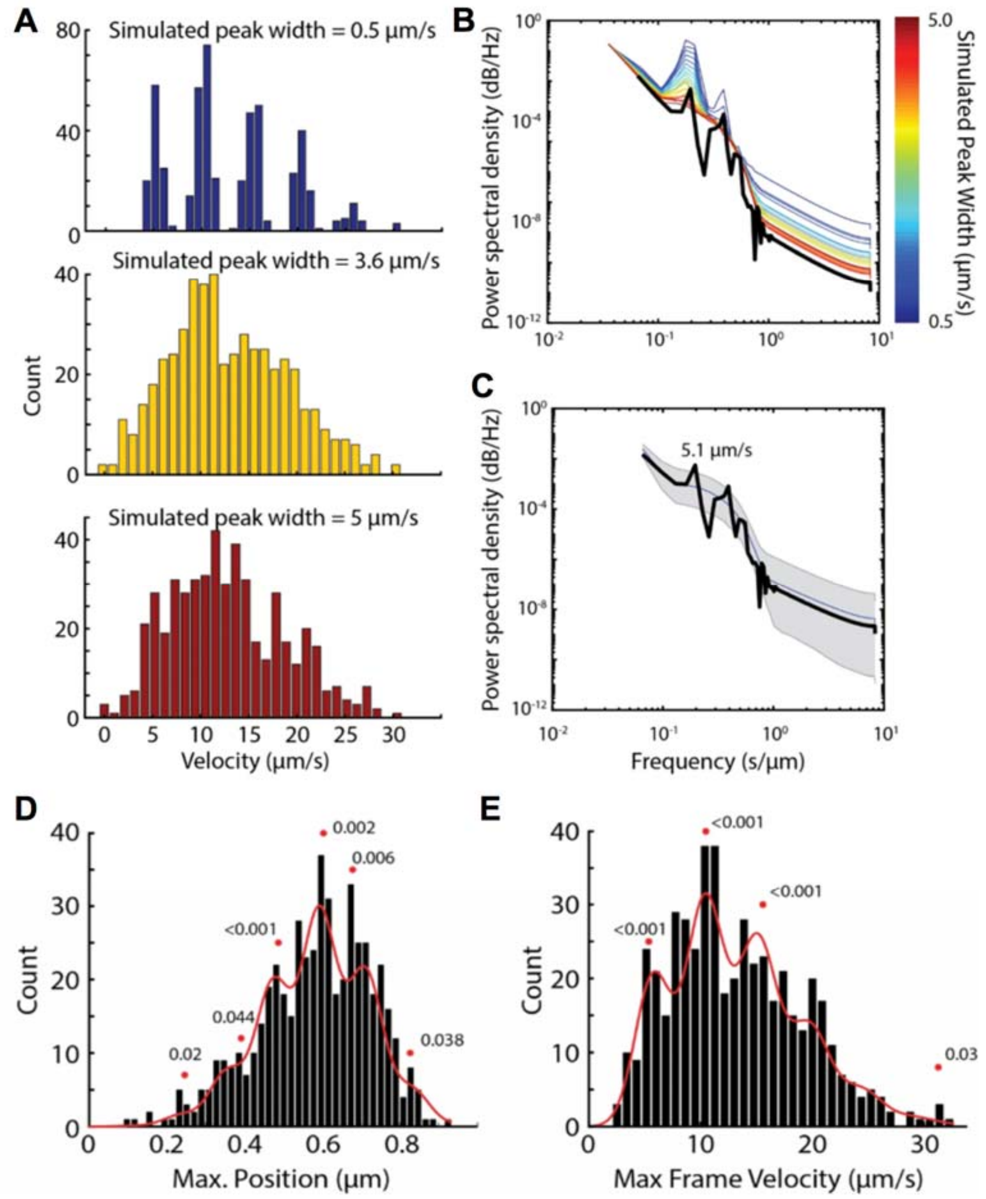

Figure S5: A) Simulated multimodal velocity distributions using the indicated peak width and a peak fixed at 5.1 µm/s. Colors correspond to colored curves in (B). B) Simulated distributions were generated with a peak spacing of 5.1 µm/s and peak widths ranging from 0.5 to 5 µm/s. For each peak width, 50 independent distributions were generated with 500 data points each and the average power spectrum for each is plotted with the indicated color. Overlaid on top in black is the power spectrum of experimental velocity distribution (Fig. 2C of main text). C) The experimental power spectrum (black) is over overlaid on the mean power spectrum of a unimodal fit to data (blue curve, gray indicating 90% confidence interval by bootstrapping). D) Gaussian mixture model fit curve with a peak spacing of 119 nm (red) overlaid on the jump size distribution (black, Fig. 2B in main text). Red asterisks indicate the modes found statistically significant by the nonparametric test and the p values are shown. E) Gaussian mixture model fit curve (red) overlaid on the velocity distribution (black, Fig. 2C in main text). Red asterisks indicate the statistically significant modes and the p values are shown.

Statistical significance of modes:

We then used two different established methods to ascertain the statistical significance of the possible modes in the data. First, we then used a nonparametric approach (10, 11) to specifically test the statistical significance of the modes in the data. This approach found statistically significant peaks (p value < 0.05) in the jump size data at the following locations: 246 nm, 392 nm, 487 nm, 603 nm, 679 nm, 827 nm. A red asterisk indicates the location of each peak in Fig. S4D and the corresponding p values are listed above each peak. We note that this peak identification approach is nonparametric and the exact peak locations are sensitive to noise in the data. However, the peak locations are close to the modes identified in the above analysis and gave a mean peak spacing of 116 nm. Similarly, for the maximum frame velocity distribution, we find significant peaks at 5.4, 10.5, 15.6, and 31.3 μm/s (Fig. S4E) and the mean peak spacing is 5.1 μm/s.

Next, we used the Silverman's test for multimodality (12), which identified the three most prominent peaks in the distribution located at 486, 601, and 682 nm for the jump size distribution at a level of $p < 0.05$. For the velocity distribution, three peaks are also identified at 10.6, 19.5, and 31.1 μm/s. We note that the Silverman's test has been found to be quite conservative, and can miss peaks particularly in the case of variable peak amplitudes (10, 13), as is the case in the data herein.

Supporting References:

1. Chowdary, P. D., D. L. Che, K. Zhang, and B. Cui. 2015. Retrograde axonal NGF transport - Motor coordination in the unidirectional motility regime. Biophys J 108:2691-2703.
2. Jaqaman, K., D. Loerke, M. Mettlen, H. Kuwata, S. Grinstein, S. L. Schmid, and G. Danuser. 2008. Robust single-particle tracking in live-cell time-lapse sequences. Nat Meth 5:695-702.
3. Ghosh, R. N., and W. W. Webb. 1994. Automated detection and tracking of individual and clustered cell surface low density lipoprotein receptor molecules. Biophys J 66:1301-1318.
4. Chowdary, P. D., D. L. Che, L. Kaplan, O. Chen, K. Pu, M. Bawendi, and B. Cui. 2015. Nanoparticle-assisted optical tethering of endosomes reveals the cooperative function of dyneins in retrograde axonal transport. Scientific Reports 5:18059.
5. Kunwar, A., S. K. Tripathy, J. Xu, M. K. Mattson, P. Anand, R. Sigua, M. Vershinin, R. J. McKenney, C. C. Yu, A. Mogilner, and S. P. Gross. 2011. Mechanical stochastic tug-of-war models cannot explain bidirectional lipid-droplet transport. Proc Natl Acad Sci U S A 108:18960-18965.
6. McKenney, R. J., M. Vershinin, A. Kunwar, R. B. Vallee, and S. P. Gross. 2010. LIS1 and NudE Induce a Persistent Dynein Force-Producing State. Cell 141:304-314.
7. Ori-McKenney, K. M., J. Xu, S. P. Gross, and R. B. Vallee. 2010. A cytoplasmic dynein tail mutation impairs motor processivity. Nat Cell Biol 12:1228-U1256.
8. Erickson, R. P., Z. J. Jia, S. P. Gross, and C. C. Yu. 2011. How Molecular Motors Are Arranged on a Cargo Is Important for Vesicular Transport. PLoS Comput. Biol. 7:22.
9. Rai, A. K., A. Rai, A. J. Ramaiya, R. Jha, and R. Mallik. 2013. Molecular Adaptations Allow Dynein to Generate Large Collective Forces inside Cells. Cell 152:172-182.
10. Minnotte, M. C. 1997. Nonparametric testing of the existence of modes. Ann. Stat. 25:1646-1660.
11. Minnotte, M. C., and D. W. Scott. 1993. The Mode Tree: A Tool for Visualization of Nonparametric Density Features. J. Comput. Graph. Stat. 2:51-68.
12. Silverman, B. W. 1981. Using kernel density estimates to investigate multimodality. J. R. Stat. Soc. Ser. B-Methodol. 43:97-99.
13. Hall, P., and M. York. 2001. On the calibration of Silverman's test for multimodality. Stat. Sin. 11:515-536.